44th AIAA Aerospace Sciences Meeting and Exhibit, Jan 9–Jan 12, Reno, Nevada

Assessment of Numerical Methods for DNS of Shockwave/Turbulent Boundary Layer Interaction

M. Wu*and M.P. Martin†

Mechanical and Aerospace Engineering Department

Princeton University, Princeton, NJ 08540

Various candidate sources of error for the discrepancy between previous direct numerical simulation (DNS) results of Wu et al.[1] and experimental data of Bookey et al.[2] are investigated. Deficiencies of current numerical methods for DNS of shockwave/turbulent boundary layer interactions (STBLI) are found. The weighted-essentially-non-oscillatory (WENO) method is improved by adding limiters in the smoothness measurement. In turn, the numerical dissipation is significantly reduced. For the compression ramp case, using the limiter results in increased size of the separation bubble and improved mean wall-pressure distribution. In addition, a fourth-order low-dissipation Runge-Kutta method is found to give less dissipation than the typically used third-order low-storage Runge-Kutta method. Combining the limiter with the low-dissipation Runge-Kutta method gives better results. Good agreement is found for the size of the separation bubble and the wall-pressure distribution when comparing against the experimental data at the same conditions.

I. Introduction

Shockwave/turbulent boundary layer interactions raise great challenge to current numerical methods. There are on-going efforts on computing STBLI problems using RANS (Reynolds Average Navier-Stokes Simulation), LES (Large Eddy Simulation) and DNS.[3–5] However, there is no numerical simulation that can predict this kind of problems precisely. RANS predicts the mean wall pressure distribution fairly well. However, it does not reproduce the unsteady nature of the shock or the heat fluxes accurately.[6,7] As for DNS and LES, they reproduce the unsteadiness in STBLI problems. However, there is no DNS that predicts the mean wall-pressure distribution accurately.[5] DNS of a 24 degree compression ramp case with $Re_\theta = 2400$ and $M = 3$ for the incoming boundary layer was first performed by Wu and Martin in 2004.[8] This configuration is shown in Figure 1. Later comparison with experiments from Bookey et al.[2] and Selig[9] shows good agreement in the velocity profile of the incoming boundary layer, the structure angle of the incoming boundary layer and the mass flux amplification through the interaction.[1] However, the mean wall-pressure distribution does not show a plateau in the DNS result,[1] as shown in Figure 2. In addition, the size of the separation bubble is significantly smaller than that in the experiment.

Studying the discrepancies that are found in the comparison of experiments and simulations at the same conditions[1] and considering the sources of disagreement, we conclude the following. (i) Code validation excludes bugs in the computational code. (ii) Inaccuracies in the incoming boundary layer are excluded on the basis of finding good agreement between the DNS and experimental data, including agreement in the

*Graduate Student, Student Member AIAA.

†Assistant Professor, Member AIAA.

	Re_θ	θ (mm)	δ^* (mm)	C_f	δ_{99} (mm)
Experiment[2]	2400	0.43	2.36	0.00225	6.7
DNS (old)[1]	2550	0.45	2.10	0.00197	7.5
DNS (new)	2100	0.38	1.81	0.00210	6.5

Table 1. Conditions for the incoming turbulent boundary layer at Mach 2.9.

skin friction coefficient, mean velocity profile and turbulent structure angles. (iii) Insufficient number of time samples is also excluded by performing a statistical convergence study. (iv) Finally, performing parametric studies of the numerical method, we find that the main source of inaccuracy is numerical dissipation.

In this paper, we present supporting evidence that excludes the possibilities (i) through (iii) above. In addition, we describe the sources of dissipation within the numerical method and show how these can be mitigated.

II. Flow Configuration and Numerical Method

The flow configuration is shown in Figure 1. The turning angle for the compression ramp is 24 degrees and the properties of the incoming turbulent boundary layer are listed in Table 1. Figure 3 shows the computational domain. The corner is 8δ downstream from the inlet, where δ is the thickness of the boundary layer at the inlet. The length along the ramp is 7δ. The wall-normal and spanwise directions are 4.5δ and 2δ in length, respectively.

The base numerical method is a 3rd-order accurate WENO method for the convection terms. We compare this method against other WENO methods with various order of accuracy, bandwidth properties and stencil adaption mechanisms in later sections. A 4th-order accurate central standard method is used to compute the viscous terms. The base time integration method is a 3rd-order accurate low-storage Runge-Kutta method. We also compare it with a 4th-order accurate low-dissipation Runge-Kutta method.

The rescaling method developed by Xu & Martin[10] is used to generate the inflow conditions. The sponge layer technique[11] combined with supersonic outflow boundary conditions is used at the outlet. On the top boundary, supersonic exit boundary conditions are also used. As for the wall boundary, we use non-slip conditions and the wall is set to be isothermal. Details about initial and boundary conditions can be found in the references.[1,8]

III. Code validation

First, we consider the Shu-Osher's problem with initial conditions $u = 0$, $p = 1$, and $\rho = 1 + 0.2sin(5x)$ for $x \geq -4.0$ and $u = 2.63$, $p = 10.33$, and $\rho = 3.86$ for $x < -4.0$. Figure 4 plots the results at t=1.8 using 200 grid points. The numerical converged result using Jiang & Shu's WENO method[12] is also plotted. The agreement validates the code for this problem.

A more stringent test case is a shockwave/laminar boundary layer interaction case. We consider a configuration that is similar to our DNS ramp case. The angle of the ramp is now 11^o, the Mach number of the incoming flow is 2.64, and the Reynolds number of the incoming boundary is $Re_L = 1.4 \times 10^5$, where L is the distance between the leading edge of the flat plate and the ramp corner. Freestream and supersonic exit conditions are used at the inlet and outlet, respectively. Figure 5 shows the wall-pressure distribution computed using our code and that found in experiments at the same conditions.[13] The plateau region in the wall pressure distribution is well predicted.

IV. Incoming Boundary Layer

It is known that the shape of the incoming boundary layer profile affects the size of the separation bubble. Figure 6 plots the comparison of the Van-Driest transformed mean velocity profile between DNS and experiment. The agreement is good except for the near wall region, where the experimental data are not expected to be accurate. The DNS results also agree well with the log law in the logarithmic region. The DNS gives the skin friction coefficient $C_f = 0.002$ while the experiments give $C_f = 0.00225$. The difference is about 12%. The structure angles in the incoming boundary are measured by computing the two-point autocorrelations of mass flux fluctuations. Figure 7 plots the structure angles for the incoming boundary layer in the DNS and experiment. The agreement is good.

V. Sample Size

In this section, we assess the validity of the sample size used to compute the mean wall-pressure distribution. Selig's experiments[9] show that the wall-pressure signal contains a high frequency and a low frequency part. The PDF of the wall-pressure signal from the experiments can be used to compute how much time the signal spends in high frequency or low frequency part of the spectra. For example, the fraction of samples spent on the low frequency part is given by:

$$R_{LF} = \frac{A_{LF}}{A_{LF} + A_{HF}} \tag{1}$$

where A_{LF} and A_{HF} are the area of the low and high frequency part in the wall-pressure signal PDF, respectively. Using the energy spectra of the wall-pressure signal from the experiment, we regenerate the fluctuating wall-pressure signal. The regenerated high and low frequency signals are plotted in Figure 8. We then sample the signals and get the minimal sample times, τ_{LF} and τ_{HF}, for which the errors of the computed RMS values are within 1% of those predicted in the experiment. Then, the minimal sample time to compute accurate statistics is:

$$\tau_s = \frac{max(\tau_{LF}, \tau_{HF})}{min(R_{LF}, R_{HF})} \tag{2}$$

Using the above procedure, the minimal sample time required for 1% error is about $100\delta/U_\infty$. Figure 9 plots the mean wall-pressure distribution computed using $35\delta/U_\infty$ and $90\delta/U_\infty$ for the DNS of Wu et al.[1] There is no noticeable difference between the results.

VI. WENO Numerical Dissipation

In WENO schemes, the numerical flux is approximated by a linear combination of candidate fluxes. Each candidate flux is given a weight based on the local smoothness of the data contained by that stencil. Stencils that span large flow field gradients are assigned small weights. In completely smooth regions, weights revert to the optimal values, where optimal is defined by, eg. maximum order of accuracy or maximum bandwidth resolution. This local adaption mechanism makes WENO schemes inherently nonlinear. Thus, the numerical dissipation in WENO methods comes from (i) the linear part of the scheme, the optimal stencil, and from (ii) the adaption mechanism, which drives the stencil away from the optimal one when non-smooth data are present.

As it is mentioned in Section III, we use a bandwidth-optimized symmetric WENO scheme[14] to compute the convective fluxes. For this scheme, Figure 10 is a sketch of the candidate stencils used to compute the flux at the $j+1/2$ grid point. There are four candidate stencils and each candidate stencil has three points. Thus, we denote this scheme by WENO3. The WENO3 method is designed to have high-bandwidth resolution and low dissipation when the optimal stencil is used, meaning that the linear part of the dissipation is optimized.

The nonlinearity index, which was first introduced by Weirs[15] and defined by Equation 3, is a measurement of how much adaption is involved in WENO.

$$NI = \left[\sum_{k=0}^{r} \left(\frac{\frac{1}{r+1} - \frac{\alpha_k / C_k^r}{\sum_{k=0}^{r} (\alpha_k / C_k^r)}}{\frac{1}{r+1}} \right)^2 \right]^{1/2} \tag{3}$$

If $NI = 0$, the optimal weights are used. This is desirable in regions without discontinuities because the optimal stencil gives the maximal bandwidth resolution and low dissipation. Figure 11 plots the nonlinearity along a grid line in the streamwise direction in a DNS of the compression ramp case. It shows that the nonlinearity index is always greater than zero, indicating that the optimal stencil is rarely used.

Figure 12 plots the result of the 1D wave equation using WENO3 with the smoothness measurement turned off and on after 10 domain-run-through times. The resolution of the sinusoidal wave is 6 points per wavelength, representing a typical short wave in DNS. With adaption off, the optimal stencil is used and the numerical result agrees well with the analytical solution. With adaption on, the WENO smoothness measurement is engaged. The numerical result shows that the amplitude of the wave is dissipated significantly. Thus, the local smoothness measurement of the WENO3 scheme wrongly engages the adaption mechanism in the vicinity of smooth short waves.

The numerical dissipation can be reduced by increasing the resolution. This can be done for simpler problems such as isotropic turbulence or turbulent boundary layers where the WENO3 gives accurate results.[16,17] In STBLI increasing the grid size to compensate for the numerical dissipation inherent in WENO3 is not feasible. Instead, we use limiters in the WENO smoothness measurement to further control the WENO adaption mechanism. The WENO smoothness measurement is defined as:

$$IS_k = \sum_{m=1}^{r-1} \int_{x_{j-1/2}}^{x_{j+1/2}} (\Delta x)^{2m-1} \left(\frac{\partial^m q_k^r}{\partial x^m} \right)^2 dx \tag{4}$$

where r is the number of candidate stencils and q_k^r is the numerical flux computed from stencil k. If we do Taylor expansion of the WENO smoothness measurement, we get:

$$IS_k = \left(f_j' \Delta x \right)^2 \left(1 + O(\Delta x^2) \right) \tag{5}$$

Here f_j' represents the derivative of the nondimensional analytical flux at point j and is of order of one for smooth data. Thus, for smooth data the smoothness measurement should be of order Δx^2 and across discontinuities it is of $O(1)$. Jiang & Shu[12] introduce a simple absolute limiter to force WENO to use the optimal weights when IS_k is less than some threshold α. The threshold value is arbitrary and problem dependent. Taylor et al.[16] introduce a relative limiter that is more general and non-problem dependent. For the compression ramp work presented here, we choose to use a well-tuned absolute limiter with $\alpha = 0.01$. Figure 13 plots the mean wall-pressure distribution with and without the limiter. For reference, the result using the relative limiter is also plotted, although this limiter is not used in the rest of the paper. Significant difference is observed in the results. With the limiter, the mean wall-pressure distribution starts to show the plateau. Also, the size of the separation bubble is increased by about 50% for the absolute limiter.

A WENO method[16] with 5 points per stencil (denoted by WENO5) is also considered. Containing more grid points, the optimal stencil of WENO5 has better bandwidth resolution and less dissipation than that of WENO3. Figure 14 plots the mean wall-pressure distribution using the two WENO methods. No significant difference is observed, meaning the linear part of the WENO dissipation is not significant in the STBLI problem. This confirms that the major source of numerical dissipation for WENO in the DNS of STBLI comes from the nonlinear adaption mechanism.

VII. RK3 Dissipation

Performing CFL convergence studies in DNS of STBLI is not feasible. Instead, we have used the convergence studies from DNS of supersonic boundary layers, where accurate results are obtained for CFL numbers of about 0.6. It is suspected that RK3 with $CFL = 0.6$ may be too dissipative for short waves in STBLI problems. We test this hypothesis on the 1D wave equation. Figure 15 plots the numerical results after 10 domain-run-through times for a sinusoidal wave with 6 points per wave length. A 10th-order accurate central scheme is used for the convective flux term. Results of two different CFL numbers, 0.1 and 0.6 are shown. With $CFL = 0.6$, the 3rd order low-storage Runge-Kutta method is too dissipative. With $CFL = 0.1$, the result is significantly improved. Reducing the CFL number to 0.1 in the DNS means that the computation becomes 5 times more expensive. For this reason, a low-dissipation fourth-order six-stage Runge-Kutta method (denoted by RK4 in the following) of Berland et al.[18] is also considered. The results of the 1D wave equation using this method are also plotted in Figure 15. We observe that RK4 with $CFL = 0.6$ is less dissipative than RK3 with $CFL = 0.1$, with RK4 being only twice as expensive as RK3. For RK4, $CFL = 0.3$ gives less dispersion error than that with $CFL = 0.6$. Therefore, we use RK4 with $CFL = 0.3$ in the DNS of STBLI.

The mean wall-pressure distributions computed using RK3 and RK4 are plotted in Figure 16. With the low-dissipation RK4, the plateau in the wall-pressure distribution is more distinct and the size of the separation bubble is 75% of that predicted in the experiment. In addition, the new DNS and experimental data now match downstream of the interaction. Figure 17 plots the size of the separation bubble versus Reynolds number. Using the limiter in WENO3 with RK4, the size of the separation is almost doubled. The new data point lies within the experimental envelope, although it is still below the experimental data point from Bookey et al.

VIII. Conclusion and Discussion

Overall, the STBLI problem is very sensitive to numerical dissipation. For compressible flow simulation, numerical dissipation is desirable in the vicinity of discontinuities to suppress spurious oscillations and to make the simulation stable. Reducing the numerical dissipation to the minimal amount for accuracy while keeping the simulation stable is challenging. Due to large-amplitude and high-frequency fluctuations in turbulent flows, it is extremely difficult to distinguish discontinuities from fluctuations mathematically, making it difficult to minimize the numerical dissipation.

It is found that current WENO3 and RK3 methods are too dissipative for DNS of STBLI problems. Due to large-amplitude, high-frequency fluctuations in the flow field, the optimal stencil of WENO is rarely used, resulting in excessive dissipation. Adding limiters in the WENO smoothness measurement forces the optimal weights to be used when the jump across a data point is less than a certain threshold, reducing the dissipation and improving the performance of WENO. For the time integration, RK3 with $CFL = 0.6$ is also found to be too dissipative. Instead, a low-dissipation RK4 is used. New results using the limiter and the low dissipation RK4 show great improvement in the wall-pressure distribution and size of the separation bubble. We consider this degree of agreement a successful one, being the best that we can do so far.

Acknowledgments

This work is supported by the Air Force Office of Scientific Research under grant AF/F49620-02-1-0361.

References

[1]Wu, M., Taylor, E. M., and Martin, M. P., "Assessment of STBLI DNS Data and Comparison against Experiments," *AIAA Paper No. 2005-4895*, 2005.

[2]Bookey, P. B., Wu, M., Smits, A. J., and Martin, M. P., "New Experimental Data of STBLI at DNS/LES Accessible

Reynolds Numbers," *AIAA Paper No. 2005-309*, 2005.

[3]Adams, N. A., "Direct numerical simulation of turbulent boundary layer along a compression ramp at M=3 and Re_θ=1685," *J. Fluid Mech.*, Vol. 420, 2000, pp. 47–83.

[4]Rizzeta, D. and Visbal, M., "Large eddy simulation of supersonic compression ramp flows," *AIAA Paper No. 2001-2858*, 2001.

[5]Knight, D., Yan, H., Panaras, G. A., and Zheltovodov, A., "Advances in CFD prediction of shock wave turbulent boundary layer interactions," *Progress in Aerospace Sciences*, Vol. 39, 2003.

[6]Zheltovodov, A. A., "Advances and Problems in Modeling of Shockwave Turbulent Boundary Layer Interactions," *Proceedings of the International Conference on the Methods of Aerophysical Research*, 2004, pp. 149–157.

[7]Sinha, K. and Candler, G. V., "Shock and Turbulent Boundary Layer Interaction in Hypersonic Flows," *Workshop on STBLI, 43rd AIAA Aerospace Sciences Meeting and Exhibit, January*, 2005.

[8]Wu, M. and Martin, M. P., "Direct Numerical Simulation of Shockwave/Turbulent Boundary Layer Interactions," *AIAA Paper No. 2004-2145*, 2004.

[9]Selig, M. S., *Unsteadiness of Shock Wave/Turbulent Boundary Layer Interactions with Dynamic Control*, Ph.D. thesis, Princeton University, 1988.

[10]Xu, S. and Martin, M. P., "Assessment of Inflow Boundary Conditions for Compressible Boundary Layers," *Physics of Fluids*, Vol. 6, No. 7, 2004.

[11]Adams, N. A., "Direct numerical simulation of turbulent compression ramp flow," *Theoretical and Computational Fluid Dynamics*, Vol. 12, 1998, pp. 109–129.

[12]Jiang, G. and Shu, C., "Efficient Implementation of Weighted ENO Schemes," *Journal of Computational Physics*, Vol. 126, 1996.

[13]Sfeir, A. A., "Supersonic laminar boundary-layer separation near a compression corner," Tech. Rep. Report N AS-69-6, University of California, Berkeley, Aeronautical Science Division, March 1969.

[14]Martin, M. P., Taylor, E. M., Wu, M., and Weirs, V., "A Bandwidth-Optimized WENO Scheme for the Direct Numerical Simulation of Compressible Turbulence," *Submitted to Journal of Computational Physics*, 2005.

[15]Weirs, G. V., *A Numerical Method for the Direct Simulation of Compressible Turbulence*, Ph.D. thesis, University of Minnesota, 1998.

[16]Taylor, E. M., Wu, M., and Martin, M. P., "Optimization of Nonlinear Error Sources for Weighted Essentially Non-oscillatory Methods in Direct Numerical Simulations of Compressible Turbulence," *AIAA Paper No. 2006-1091*, 2006.

[17]Martin, M. P., "Hypersonic Turbulent Boundary Layers: Understanding the Physics to Perform Accurate Complex Simulations," *AIAA Paper No. 2004-2337*, 2004.

[18]Berland, J., Bogey, C., and Bailly, C., "Low-dissipation and low-dispersion fourth-order Runge-Kutta algorithm," *Computers and fluids*, Vol. to appear, 2005.

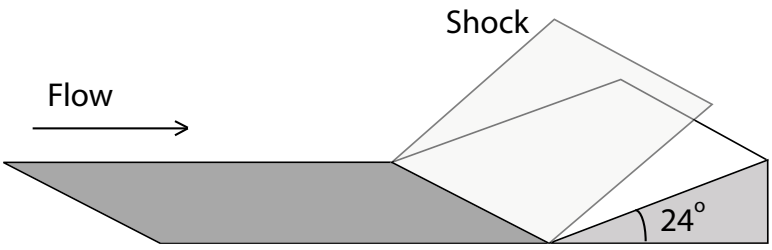

Figure 1. Configuration of the compression ramp case.

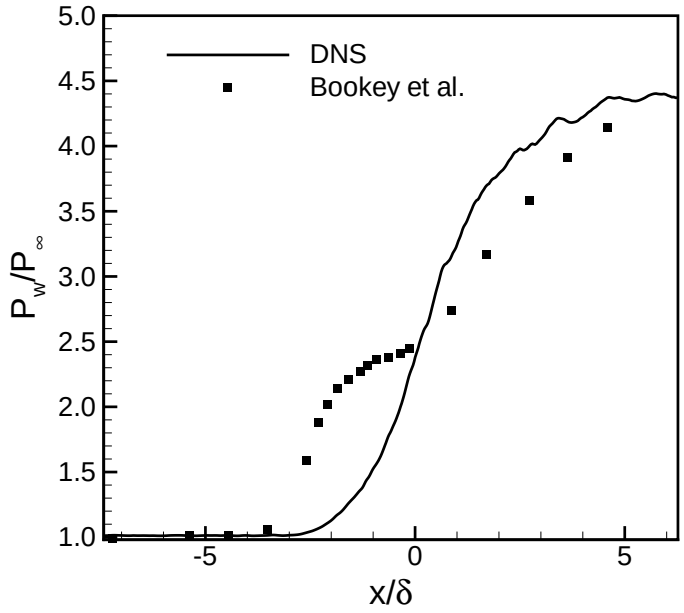

Figure 2. Discrepancy between DNS[8] and experiment[2] in the mean wall-pressure distribution for the compression ramp case.

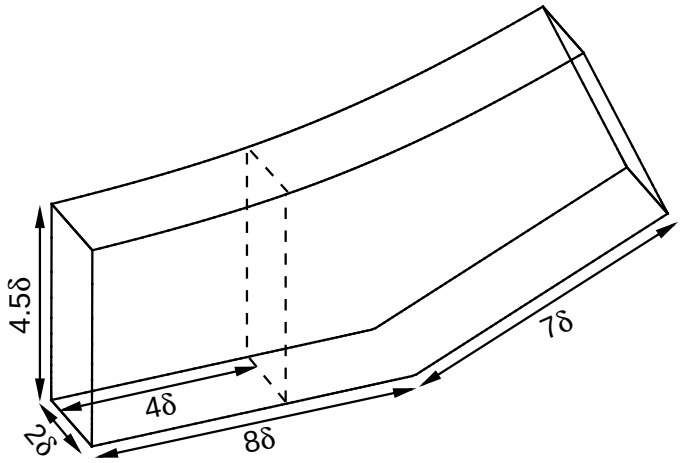

Figure 3. Computational domain of the compression ramp case.

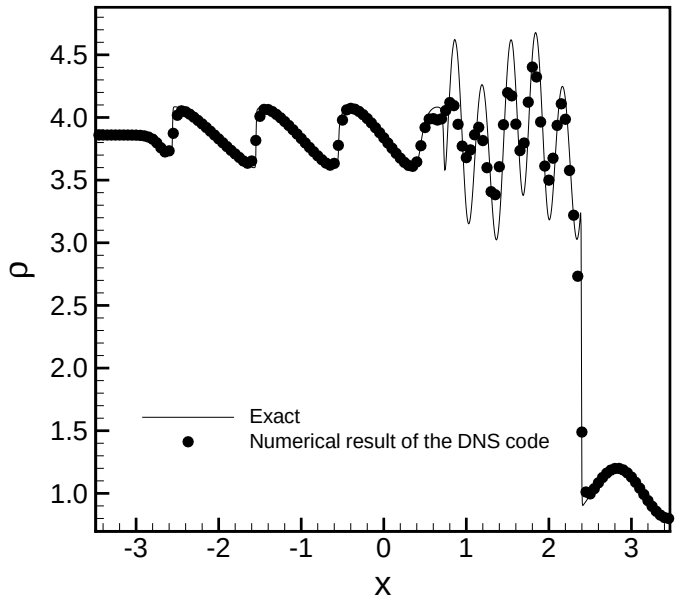

Figure 4. Computed density at t=1.8 for the Shu-Osher's problem.

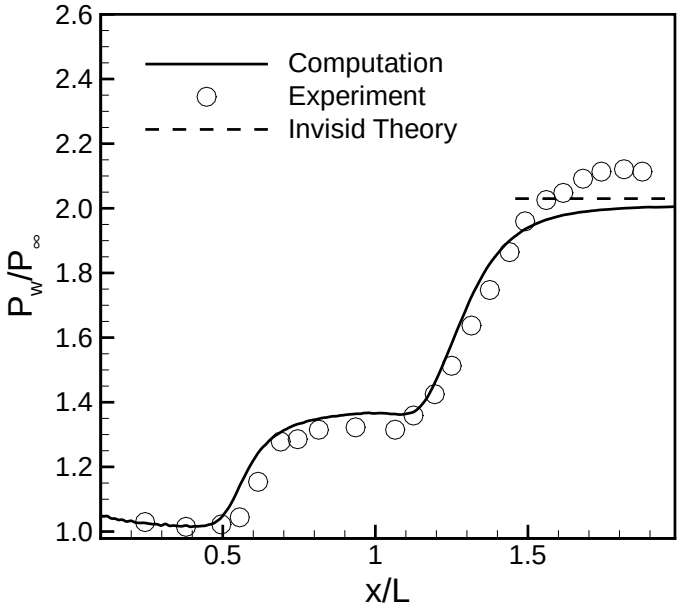

Figure 5. Wall pressure distribution for the ramp case with laminar incoming boundary layer.

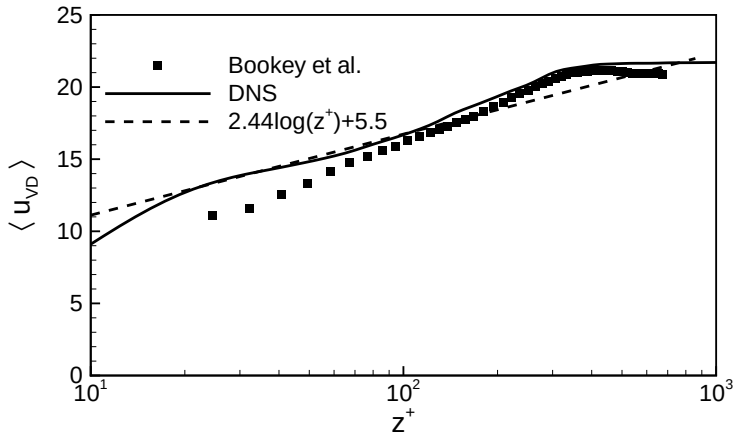

Figure 6. Comparison of the Van-Driest transformed mean velocity profile between DNS[8] and experiment.[2]

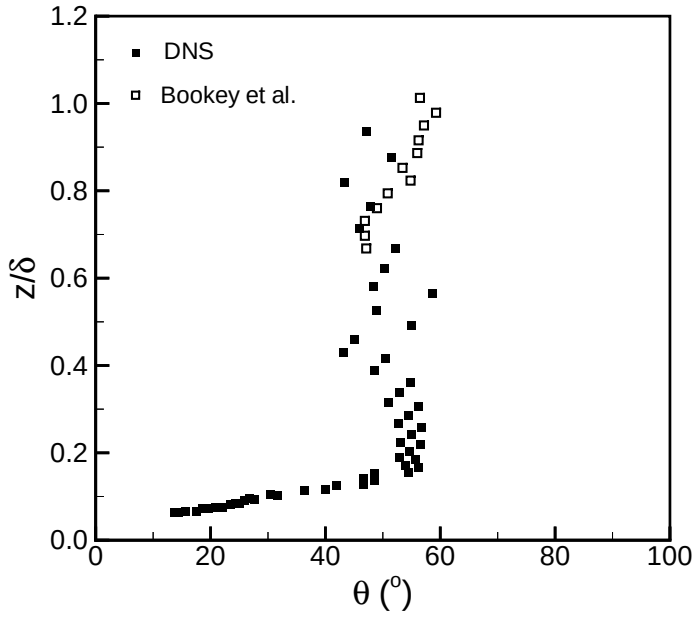

Figure 7. Comparison of the structure angles in the incoming boundary layer between DNS[8] and experiment.[2]

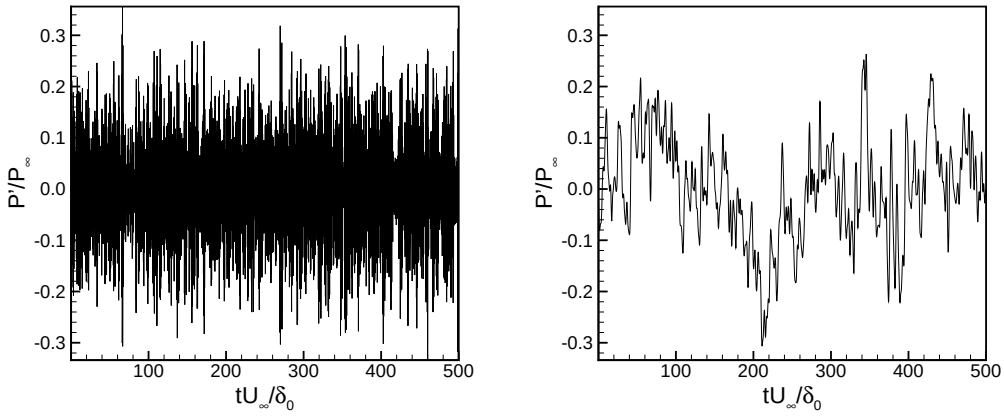

Figure 8. Regenerated wall pressure signal: (a) high frequency part and (b) low frequency part.

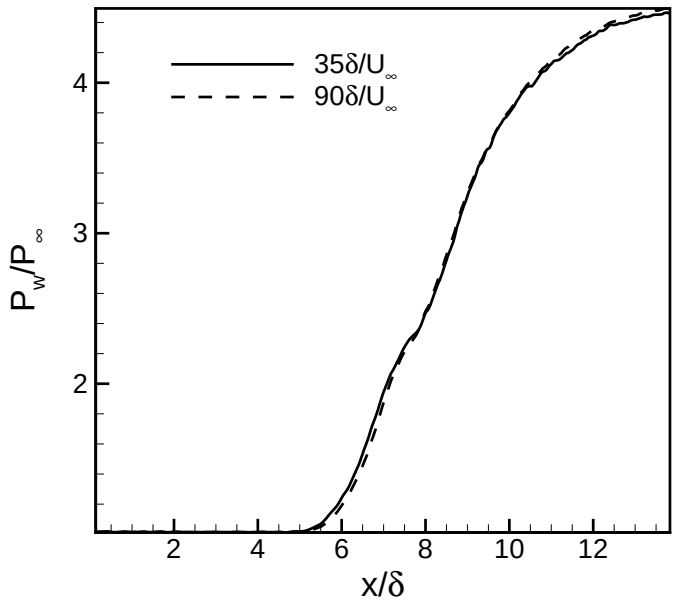

Figure 9. Mean wall-pressure distribution computed using different sample time.

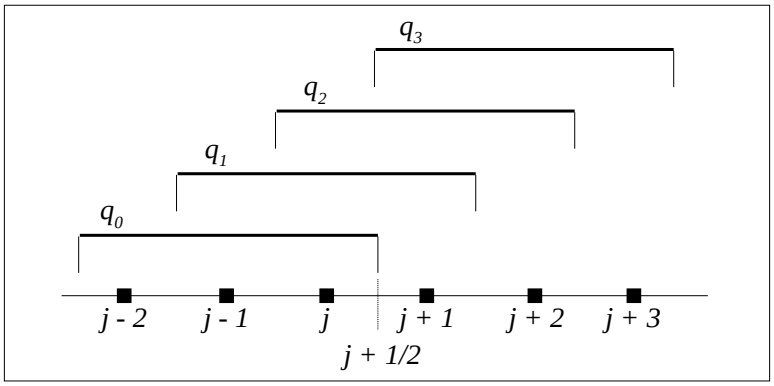

Figure 10. Sketch of the WENO candidate stencils.

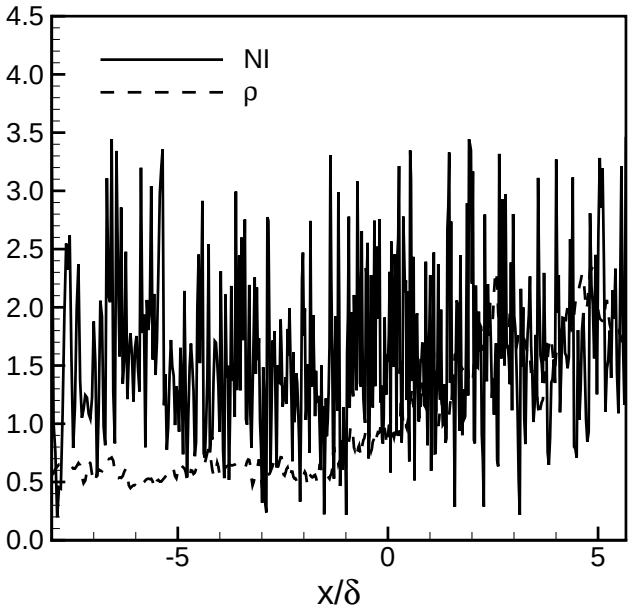

Figure 11. Nonlinearity index along a grid line in the streamwise direction in the ramp case.

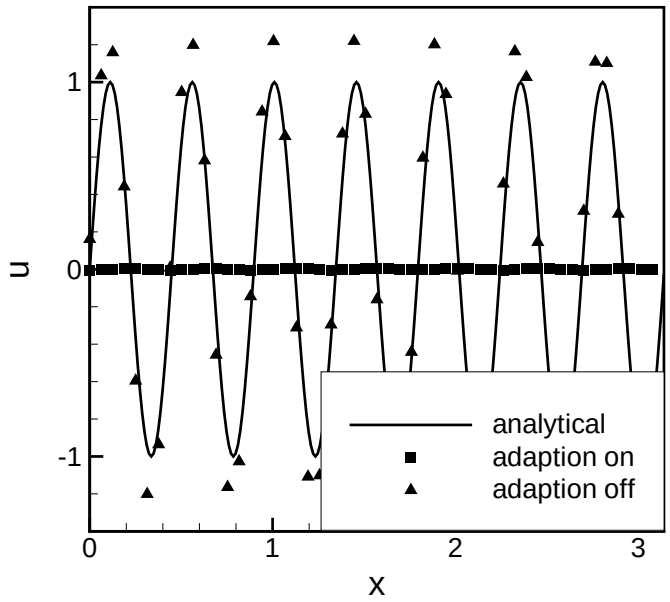

Figure 12. Numerical results of the 1D wave equation with and without the WENO smoothness measurement.

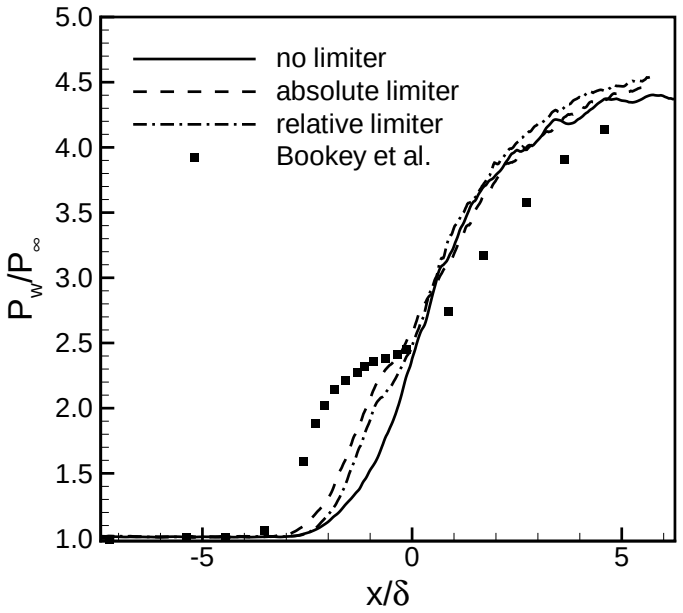

Figure 13. Mean wall-pressure distribution computed with and without the limiter compared with experiment.[2]

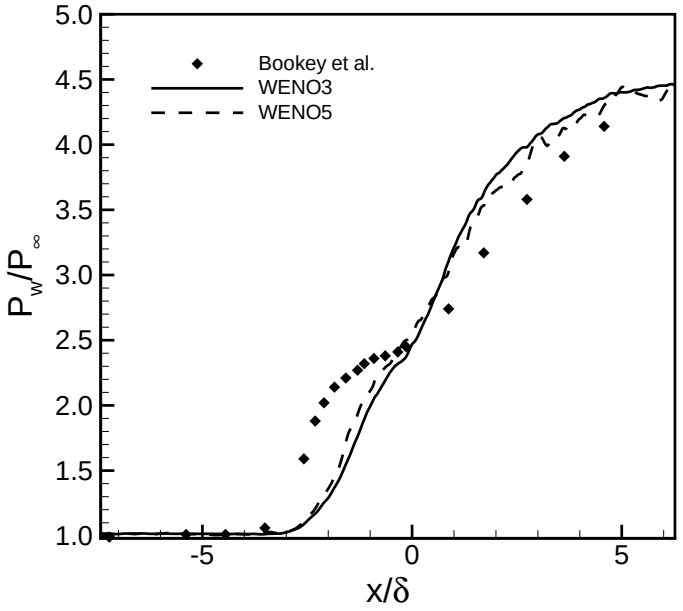

Figure 14. Mean wall-pressure distribution computed with WENO3 and WENO5.

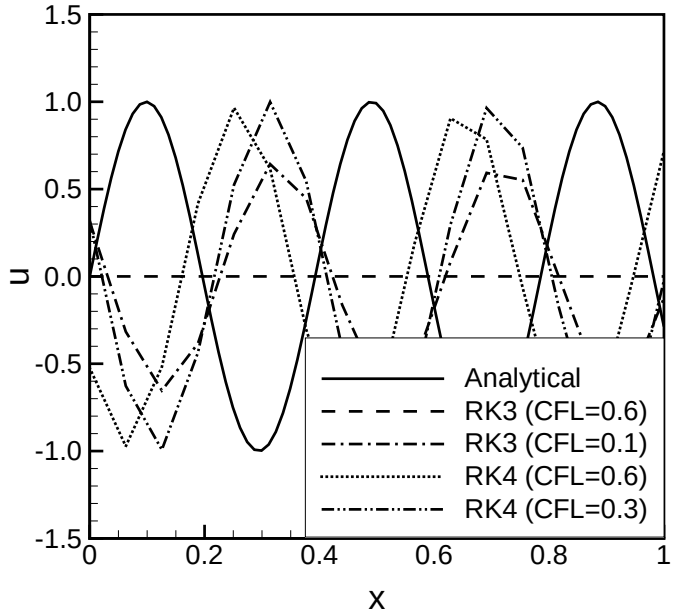

Figure 15. Numerical solution of the 1D wave equation using RK3 and RK4 with varying CFL numbers.

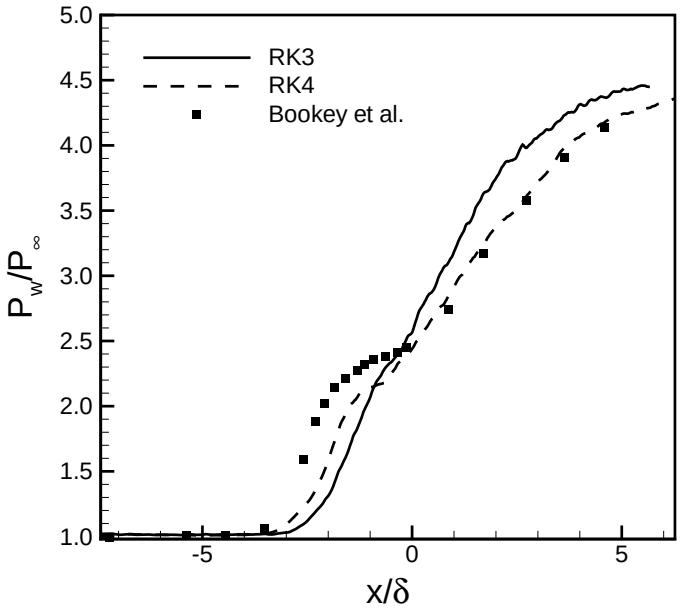

Figure 16. Mean wall-pressure distribution computed with WENO limiter and RK4 compared with experiment.[2]

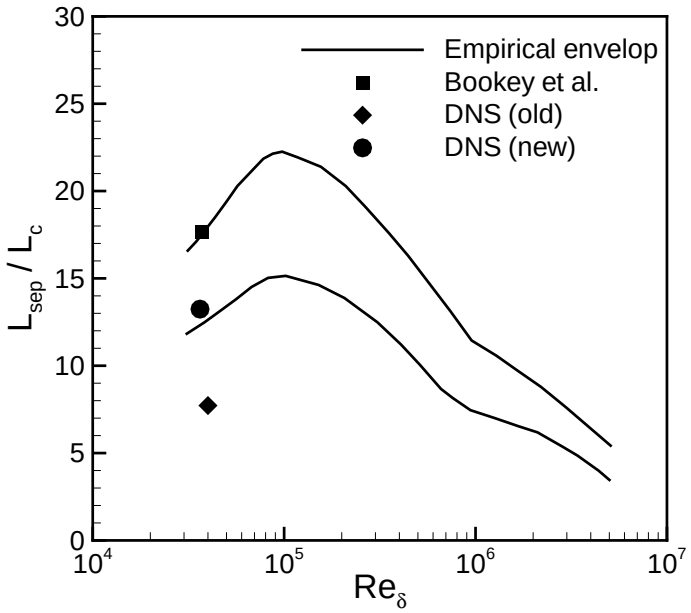

Figure 17. Comparison of the size of the separation bubble between the new and old DNS results.